Dispersion-Suppressed Mode Depletion by Exceptional Points for On-Chip Nonlinear Optics

Boqing Zhang,[1,§] Nuo Chen,[1,§] Haofan Yang,[1] Yuntian Chen,[1,2,*] Jianji Dong,[1,2] Heng Zhou,[3] Xinliang Zhang,[1,2,†] and Jing Xu[1,2,‡]

[1] *School of Optical and Electronic Information, Huazhong University of Science and Technology, Wuhan 430074, China*

[2] *Wuhan National Laboratory for Optoelectronics, Huazhong University of Science and Technology, Wuhan 430074, China*

[3] *Key Lab of Optical Fiber Sensing and Communication Networks, University of Electronic Science and Technology of China, Chengdu 611731, China*

(Received 21 July 2021; revised 20 July 2022; accepted 3 August 2022; published 12 September 2022)

Dispersion-suppressed mode depletion in a resonant cavity is usually challenging due to the entanglement of amplitude and phase response dictated by the Kramers-Kronig relationship. In this study, we examine the dispersion-suppressed mode depletion induced by parity–time- (*PT*-) symmetric dual resonators by taking advantage of the exotic property at the exceptional point (EP). We show that this technique can modify the linear spectrum of an optical resonator for relaxed phase-matching conditions in nonlinear optics, thus profoundly altering the nonlinear behavior of integrated Kerr combs. Indeed, dissipation-induced modulation instability (MI) is predicted and numerically verified in normal group-velocity dispersion (GVD) microresonators, and the single-soliton-generation probability is greatly enhanced in the anomalous GVD regime. The merging of two vibrant disciplines, i.e., non-Hermitian optics and nonlinear optics, especially Kerr microcombs, can deepen our understanding of non-Hermitian optical frequency combs and opens broad applications ranging from fiber-optic communications, microwave photonics, and ultrafast optics to quantum state manipulations.

DOI: 10.1103/PhysRevApplied.18.034028

On-chip nonlinear optics is promising for classical and nonclassical applications [1–7] but is usually hindered by phase-matching conditions [8], which are required for efficient interactions between the waves involved. As an important application of integrated nonlinear optics, Kerr microcombs emerge as the linear phase mismatch compensates for the nonlinear phase mismatch offered by the strong pump light, which exists only in the anomalous dispersion regime. Notably, anomalous dispersion for devices designed for the near-infrared wavelength range requires thick films that require challenging fabrication processes [9]. Recent works show that frequency-dependent loss (i.e., optical filtering) can induce additional phase mismatch that cancels out the sum of the linear and nonlinear phase mismatch in the normal dispersion regime, leading to nonlinear optical gains [10–12] that are responsible for the generation of microcombs if embedded in optical cavities.

However, pure mode depletion in resonant cavities is hindered by the Kramers-Kronig relationship, i.e., new resonances are generated due to the mutual coupling between the amplitude and phase responses through the periodic boundary condition of the cavity. This is true even for intracavity-mode-depletion effects induced by all-optical means [13–16]. As a result, optical frequency combs based on optical filtering in the normal dispersion regime are demonstrated in fiber-based cavities, yet with the frequency spacing between adjacent comb lines deviating from the pure filtering effect due to additional dispersion effects [17]. More importantly, the deviations in microresonators become qualitatively different from the bulk cavities, since the dispersion in microresonators can be orders of magnitude larger than that of their bulk counterparts, satisfying phase-matching conditions by reversing the linear phase-matching sign [9,18–20] and completely overriding loss-induced phenomena. Therefore, it is critical to develop a simple and effective strategy to realize a dispersion-suppressed mode-depletion method for on-chip intracavity mode manipulation.

Recent explorations of parity–time- (*PT*-) symmetric coupled waveguides and resonators open the doors for non-Hermitian light manipulation [21–23]. Exceptional

*yuntian@hust.edu.cn
†xlzhang@hust.edu.cn
‡jing_xu@hust.edu.cn
§B. Zhang and N. Chen contributed equally to this work.

points (EPs) are utilized to induce topological chirality [24,25], enhance sensitivity [26], or for the Sagnac effect [27,28]. Novel microcomb dynamics in *PT*-symmetric coupled microrings with modifications to all resonant modes have also been investigated [29,30]. Various schemes of light manipulation based on coupled microresonators have also been reported, yet the underlying systems are Hermitian [9,18–20]. Here, we explore the EP of dual coupled microresonators to design dispersion-suppressed mode depletion for a single resonant mode. Due to the simultaneous collapse of eigenvalues and eigenvectors at the EP, unsplit but significantly increased dissipation of the selected resonance is achieved, fitting the requirement of pure mode depletion elegantly. By taking advantage of relaxed phase-matching conditions offered by pure mode depletion, dissipation-induced modulation instability (MI), as well as induced dark pulses, are theoretically predicted in microresonators. In addition, we identify dispersion-suppressed mode depletion as a route towards harnessing single dissipative Kerr soliton generation with a high generation probability in the anomalous dispersion regime, a phase-matching-irrelevant method that is distinct from the dispersive-wave-induced losses, meanwhile featuring improved system controllability and robustness.

We start from coupled-mode theory (CMT) [31] to demonstrate the idea of dispersion-suppressed mode depletion. It is well known that the intracavity intensity enhancement of a single microresonator, defined as the ratio between the intracavity mode intensity and input mode intensity, yields a comb spectrum [Fig. 1(a)]. To get rid of the intensity enhancement of a particular resonance at ω_1 of the main resonator (red, low loss), an auxiliary microresonator (blue, high loss), the resonant frequency, ω_2, of which is tuned to ω_1 can be used, forming a non-Hermitian system, as sketched in Fig. 1(b). The intrinsic decay rates of two resonators are denoted by γ_1 and γ_2, and $\gamma_1 \ll \gamma_2$. The coupling decay of the main cavity induced by the straight waveguide is γ_c. The coupling rate between the two cavities is κ. To achieve single-mode selectivity, the radius of the auxiliary ring is much smaller than that of the main ring. $|a_1|^2$ and $|a_2|^2$ are the stored energies inside the main and auxiliary cavities, respectively. In the regime of $\gamma_c \leq \gamma_1$ (i.e., the main cavity is in the undercoupling or critical coupling condition if the auxiliary cavity is absent), the evolution of the modal field, $A = (a_1, a_2)^T$, in this structure obeys $idA/dt = HA - i\sqrt{\gamma_c}(a_0 \quad 0)^T$, where the non-Hermitian Hamiltonian, H, is given by

$$H = \begin{bmatrix} \omega_1 & \kappa \\ \kappa & \omega_2 - i\gamma_2 \end{bmatrix}. \tag{1}$$

The eigenfrequencies of H are $\omega_\pm = \omega_1 - i(\gamma_2/2) \pm (1/2)\sqrt{4\kappa^2 - \gamma_2^2}$ when $\omega_2 = \omega_1$. Figures 2(a) and 2(b) schematically plot the mode splitting and decay of the supermodes as a function of γ_2, as given by $\mathrm{Re}(\omega_\pm - \omega_1)$ and $\mathrm{Im}(\omega_\pm)$, respectively. Under the conditions of $4\kappa^2 = \gamma_2^2$, the eigenfrequencies and eigenvectors collapse and the coupled resonators operate at the EP. Figures 2(c)–2(e) show the intracavity intensity enhancements of the main cavity (solid black lines) at three different γ_2, corresponding to the *PT*-symmetric regime (i), the EP (ii), and the *PT*-symmetry-broken regime (iii), respectively. The intracavity intensity enhancements are calculated by Eq. (A2), divided by the round-trip time of the main cavity (see more information in Appendix A). It is clear that the EP [case (ii)] serves elegantly in the role of dispersion-suppressed mode depletion, while mode splitting occurs in case (i), and the intracavity intensity enhancement of the main cavity recovers in case (iii). The dispersion-suppressed mode depletion can be described quantitatively by $\eta(\omega)$, a ratio defined as the mode intensity of the main cavity in the coupled structure over that of a single cavity. From CMT analysis, $\eta(\omega)$ is found to be

$$\eta(\omega) = 1 + \frac{\kappa^2}{(\omega - \omega_+)(\omega - \omega_-)}. \tag{2}$$

It is trivial to see that $\omega_\pm \approx \omega_1 + i\gamma_2/2$ and $\eta(\omega_1) = 0$ at EP, leading to the absence of resonance splitting (dispersion suppressed) and elimination of the resonant field at ω_1 (depletion). See Appendix A for a detailed derivation.

The coupled resonators can also be analyzed by a more rigorous method, i.e., the transfer matrix method (TMM), which serves as a link between the linear analysis shown above and the nonlinear analysis discussed later. The intensity enhancement in the main cavity derived by the TMM is given by the red dashed lines in Figs. 2(c)–2(e), which agree well with the CMT results (see Table I in Appendix A for the relationships between the parameters used in the two models). In the framework of the TMM,

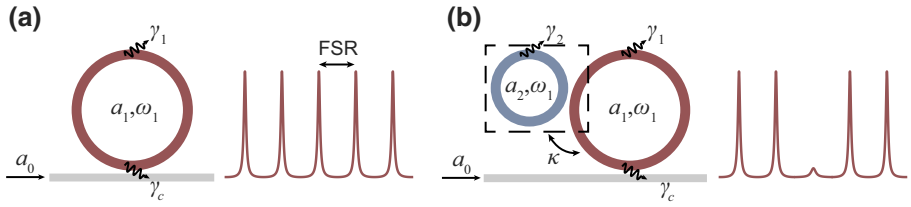

FIG. 1. Schematic diagram of (a) a conventional high-Q microresonator and (b) parity–time-symmetric coupled microrings, and the corresponding intracavity field enhancements of the main cavity.

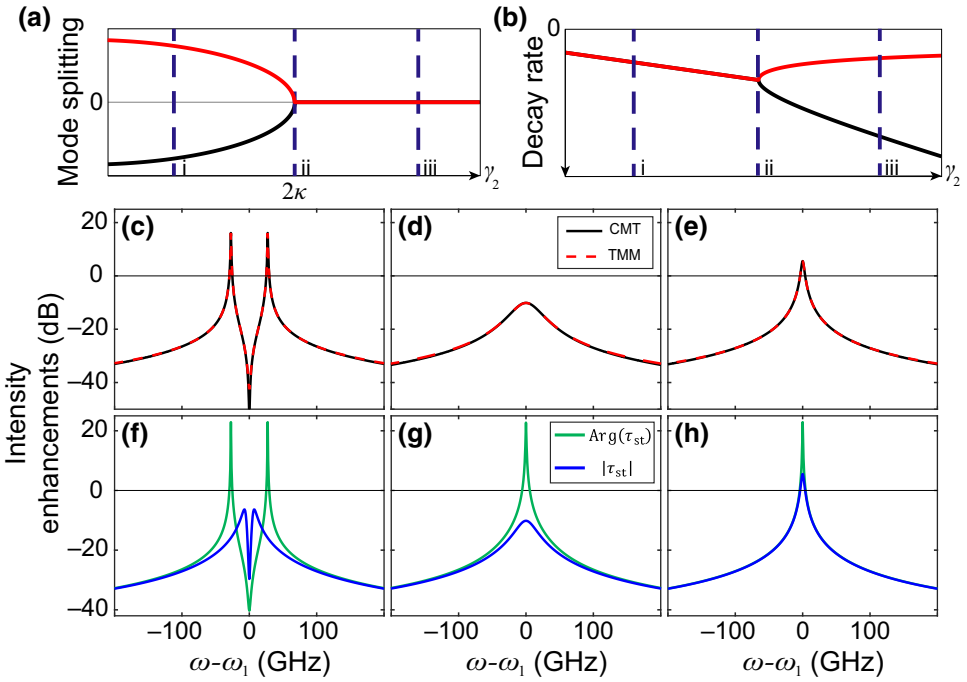

FIG. 2. Operation principle of dispersion-suppressed mode depletion. (a) Mode splitting, i.e., $\mathrm{Re}(\omega_\pm) - \omega_1$, as a function of γ_2. (i)–(iii) $\gamma_2 = 373.5$ MHz, 56 GHz, and 373.5 GHz, respectively. (b) Decay rates of the two eigenmodes, i.e., $\mathrm{Im}(\omega_\pm)$, as a function of γ_2. Red branch is the variation in the main cavity. (c)–(e) Intracavity intensity enhancements of the main cavity at three different γ_2, corresponding to (i)–(iii) in (a),(b). Black and red dotted lines are derived from CMT and the transfer-matrix method (TMM), respectively. (f)–(h) Intensity enhancements of the main cavity in TMM derived by considering the amplitude and the phase response of τ_{st} separately, corresponding to (i)–(iii) in (a),(b). Green and blue lines are simulated by considering the phase and amplitude response, respectively. Parameters used, $\gamma_1 \approx 271.65$ MHz, $\gamma_c \approx 42.45$ MHz, and $\kappa \approx 27.3$ GHz. Parameters used in TMM are calculated according to Table I given in Appendix A.

the auxiliary resonator and part of the main resonator, as shown by the dashed box in Fig. 1(b), form a subsystem, the role of which is equivalent to a lumped filter inserted into the main cavity. The transfer function of the lumped filter, $\tau_{st}(\omega)$, is given by Eq. (A6) in Appendix A. The intensity enhancements of the main cavity, derived by considering the amplitude and phase response of τ_{st}, are shown by the blue and green lines, respectively, in Figs. 2(f)–2(h). By comparing Figs. 2(f)–2(h) with Figs. 2(c)–2(e), it is clear that the amplitude and phase response of τ_{st} is responsible for the dispersive and dissipative effects, respectively.

Based on the linear property of the system, we further verify the effectiveness of the dispersion-suppressed mode depletion in nonlinear processes via explorations of the microresonator-based optical frequency combs (OFCs). It is known that self-organized dissipative Kerr solitons (DKSs) can be formed based on the double balancing of nonlinearity and dispersion as well as dissipation and parametric gain in chip-scale microresonators [32]. The nonlinear behavior is captured using a generalized version of the standard Lugiato-Lefever equation (GLLE) [12] with the lumped spectral filter τ_{st} (verification of the GLLE model is given in Appendix B). A spectral Sech^2 envelope is expected, regarding the single DKS generated in anomalous group-velocity dispersion (GVD) microresonators. Now we consider the situation in which non-Hermitian singularity is introduced into a specific longitudinal mode of the main cavity by our scheme, i.e., the third mode ($\mu = 3$) from the pump resonance ($\mu = 0$) gets depleted in this case. As shown in Fig. 3(a), a single DKS with the spectral envelope following the Sech^2 function is generated as well, except that the third comb line from the pump mode gets strongly suppressed. The comb spectra generated by considering the phase and amplitude of τ_{st} in the GLLE model are given in Figs. 3(b) and 3(c), respectively. Compared with Fig. 3(a), it is clear that dissipation other than the dispersion dominates in this process, confirming the role of pure mode depletion. Note that single-mode depletion is valid over a certain bandwidth due to the physical limitations of decreasing the radius of the auxiliary cavity. By changing the alignment of the two cavities, the mode that gets depleted can be tuned (as discussed in Appendix C). In contrast to the DKS generated by Hermitian-mode coupling, the soliton spectra generated by the dispersion-suppressed operation avoid significant envelope distortion from the Sech^2 shape [33], which remains valid even for

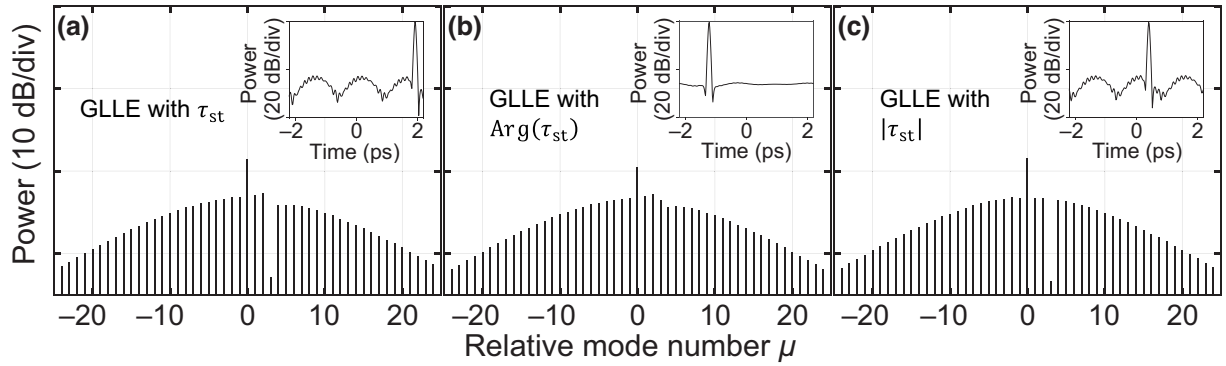

FIG. 3. Dissipative Kerr soliton with single-mode depletion in the anomalous dispersion regime. (a)–(c) Simulated spectra from GLLE with τ_{st}, Arg(τ_{st}), and $|\tau_{st}|$, respectively. Insets are the corresponding temporal waveforms of the generated single solitons. Simulation parameters are $t_{R_1} = 4.4$ ps, $L_1 = 628$ μm, $\alpha_1 = 2.4 \times 10^{-3}$, $\alpha_2 = 1 \times 10^{-2}$, $u_1 = \sqrt{3.75 \times 10^{-4}}$, $u_2 = 0.021$, $\beta_2 = -81$ ps^2/km, $\Gamma = 1$(W m)$^{-1}$, $|E_{in}|^2 = 0.42$ W, and δ scans linearly starting from -0.0041 at a sweep rate of 7.5533×10^{-7} per round-trip. L_1/L_2 is 33. See Table I in Appendix A for more descriptions of the parameters.

the generation of octave-spanning frequency combs (see Appendix D).

In addition, a significant improvement in single-soliton-generation probability is observed by our scheme compared to the case of a single cavity with the same pump-scanning rate. Figure 4 shows a diagram of the probability of single-soliton generation as a function of external pump power and pump phase detuning with and without single-mode depletion [34], showing a greatly boosted success rate of single-soliton generation to nearly 100% even at low power levels, suggesting it is insensitive to the external pump power. Single solitons are formed by fixed-speed unidirectional pump-frequency sweeping in both cases, showing a simple way to greatly improve the success rate while avoiding a complex pump-scanning trajectory [35]. The improvement in single-soliton statistics can be attributed to the temporal modulation induced by spectral filtering, indicating the effectiveness of a phase-matching-irrelevant loss mechanism (i.e., pure mode depletion other than dispersive-wave-induced loss [33]) for soliton trapping or passive mode locking. The mode at $\mu = 10$ is depleted in this case, which is similar to the case of depleting $\mu = 3$ or other modes located relatively close to the pump. Moreover, the impact of the pump-detuning rate, loss of the auxiliary cavity, coupling, periodicity of the dissipation operation, and the misalignment between two cavities are thoroughly analyzed (see Appendices E and F), showing outstanding robustness against various structural or operational imperfections. This is in contrast to dispersion-assisted soliton formation, where refined dispersion control is required [33,36].

Next, we proceed to study the impact of the dispersion-suppressed mode-depletion operation on assisting OFC generation via depletion-induced MI in normal GVD

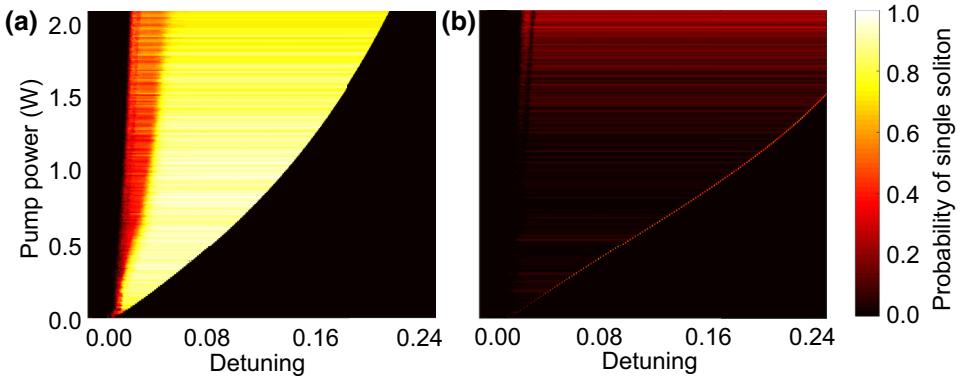

FIG. 4. Probability of single-soliton formation as a function of pump power and pump detuning with (a) and without (b) single-mode depletion in the anomalous GVD regime on the pump-detuning map. For each pump level, 100 simulations of GLLE are carried out, and the probability of the single soliton is derived accordingly [following, e.g., Fig. 6(b) in Ref. [30]]. Statistical heat map is obtained by scanning the pump from 0 to 2 W with a 0.01-W increase per step. Mode $\mu = 10$ is depleted. Parameters used are the same as those in Fig. 3.

microresonators. In general, MI is a mechanism responsible for amplification and self-organization, commonly related to amplification processes in nonlinear optics. It is known that MI in normal GVD microresonators is challenging due to the lack of effective phase matching. Several studies have employed the strong mode splitting that occurs in Hermitian-coupled microresonators to reverse the local dispersion from normal to the abnormal regime and realize MI and dark solitons in normal GVD microcavities [18,37,38]. In contrast, it is proposed and validated in fiber-based cavities [17] that frequency-selective depletion or filtering can break the limit of Hermitian phase matching [10,39] and leads to MI in the normal GVD regime. To validate the effectiveness of the dissipation-induced MI in microresonators and to distinguish such MIs from the one generated by dispersion reversing [18], the dispersion-suppressed mode-depletion operation in microcavities is essential. We consider again the situation that the third mode ($\mu = 3$) from the pump resonance ($\mu = 0$) gets depleted. The initial comb line is expected to be generated on the other side of the pump, which is located symmetrically with respect to the pump compared to the filtered frequency (i.e., $\mu = -3$). After four-wave mixing, other comb lines are generated, including the one at the mode that gets depleted [11]. As a consequence, the free spectral range (FSR) of the generated comb is determined by the relative mode number of the mode that gets depleted. As shown in Fig. 5(a), the OFC is generated with FSR equal to 3 times the FSR of the main cavity. Simultaneously, dark pulses are predicted within a round-trip time in the time domain, which has not been reported so far based on dissipation-induced MI. By changing the alignment of two cavities, the FSR of the generated frequency combs and the number of dark pulses can be tuned (see Appendix C). Note that for bulk cavities, there is a certain frequency shift between the center filtering frequency and the initially generated comb lines [17]. The reason behind this difference lies in the fact that the frequency shift induced in bulk cavities is due to phase modulation from the bulk filters [17], which is minimized in our scheme. Compared to the dissipation-induced MI in bulk cavities, the FSR of such a MI generated by our scheme can be precisely controlled. Further analyses regarding the MI threshold show that the input pump power can be substantially reduced due to the high-quality factor of integrated microresonators (see Appendix G). The comb spectra generated by considering the phase and amplitude of τ_{st} in the GLLE model are given in Figs. 5(b) and 5(c), respectively. The remarkable coherence between Figs. 5(c) and 5(a) reveals the fact that dissipation is responsible for MI in microresonators in this scenario and produces a coherent frequency comb that leads to dark pulses. Instead, the absence of sidebands in Fig. 5(b) is due to the fact that all modes remain in the normal GVD regime (Appendix H). Note that only the intracavity powers of the main cavity are shown in Figs. 3 and 5, since optical fields in the auxiliary ring are relatively weak and effective nonlinearities occur mostly in the main cavity (see the discussion in Appendix B).

In conclusion, we propose a simple and robust way to realize the dispersion-suppressed mode-depletion effect in microresonators by utilizing the simultaneous collapse of eigenvalues and eigenvectors of coupled microring resonators at the EP. The effectiveness of our scheme is verified in the contexts of both linear and nonlinear optical processes. With the tunable resonant frequency of the lossy resonator, one can thus selectively deplete any target resonance of the main ring resonators (within the tuning range of the microheaters) against the broad background comb spectra. Importantly, single-mode-selective and dispersion-suppressed mode depletion are particularly relevant for nonlinear phenomena in high-Q microresonators. With dispersion-suppressed mode depletion, dissipation-induced MI in normal dispersion microresonators is reported without suffering from the FSR deviations observed in the bulk cavities. Dark pulses, as well as tuning of the number of dark pulses,

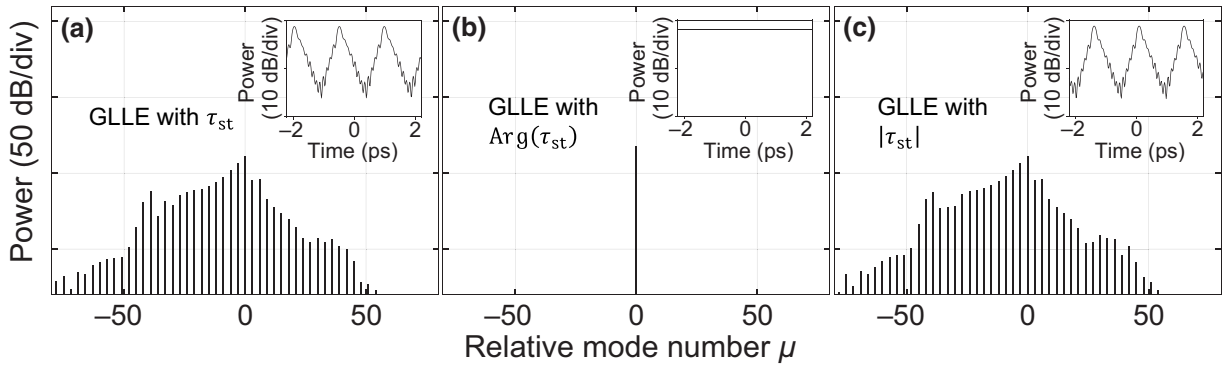

FIG. 5. Optical frequency combs with single-mode depletion in the normal dispersion regime. (a)–(c) Simulated spectra from GLLE with τ_{st}, $\mathrm{Arg}(\tau_{st})$, and $|\tau_{st}|$, respectively. Insets are the corresponding temporal waveform of the generated dark pulses. Simulation parameters are the same as in Fig. 3 except $\alpha_2 = 1.5 \times 10^{-2}$ and $\beta_2 = 190\ \mathrm{ps}^2/\mathrm{km}$.

are predicted based on dissipation-induced MI. In addition, greatly improved single-soliton-generation probability in the anomalous dispersion regime is achieved with dispersion-suppressed mode depletion instead of dispersive-wave-induced losses for passive mode locking. Thorough analyses of different parameters show that our scheme is robust against various structural or operational parameters. Our work combines studies on two frontiers, i.e., non-Hermitian optics and Kerr microcombs, which can potentially bring unforeseen opportunities for on-chip nonlinear optics. By offering a degree of intracavity mode-manipulation freedom other than dispersion engineering, we expect a significant impact not only in optics but in other resonant-related physical fields, such as acoustics, atomic physics, and mechanics.

ACKNOWLEDGMENTS

This work is supported by the National Key Research and Development Program of China (Grant No. 2019YFB 2203103).

APPENDIX A: COMPARISON OF THE POWER-COUPLING MODEL AND THE ENERGY-COUPLING MODEL

It is well known that coupled microring resonators can be analyzed by the power-coupling model, i.e., the TMM, or by the energy-coupling model, i.e., the temporal CMT [31]. Diagrams of the energy-coupling model and power-coupling model are sketched in Fig. 6. α_1 and α_2 are the intrinsic loss per round trip of the main and auxiliary cavities, respectively. u_1 and u_2 are the field coupling coefficient of the coupling region shown by the black dashed boxes in Fig. 6(a).

In the energy-coupling model, for the intracavity mode fields a_1 and a_2, and input field a_0, the rate equations for the coupled-resonator system can be written as

$$\frac{da_1}{dt} = (i\omega_1 - \gamma_1 - \gamma_c)a_1 - i\kappa a_2 - i\sqrt{2\gamma_c}a_0, \tag{A1a}$$

$$\frac{da_2}{dt} = (i\omega_2 - \gamma_2)a_2 - i\kappa a_1. \tag{A1b}$$

The intensity enhancement in the main cavity can be expressed as

$$\left|\frac{a_1}{a_0}\right|^2 = \left|-\frac{\sqrt{2\gamma_c}[(\omega-\omega_2)-i\gamma_2]}{[(\omega-\omega_1)-i(\gamma_1+\gamma_c)][(\omega-\omega_2)-i\gamma_2]-\kappa^2}\right|^2. \tag{A2}$$

Similarly, the corresponding intensity enhancement can be obtained in the case of a single cavity as $|a'_1/a_0|^2 = \left|-\left(\sqrt{2\gamma_c}/[(\omega-\omega_1)-i(\gamma_1+\gamma_c)]\right)\right|^2$, where a'_1 is the mode field in the single cavity. Therefore, the mode intensity of the main cavity in the coupled structure over that of a single cavity can be expressed as

$$\eta(\omega) = \frac{a_1}{a'_1} = \frac{[(\omega-\omega_2)-i\gamma_2][(\omega-\omega_1)-i(\gamma_1+\gamma_c)]}{[(\omega-\omega_1)-i(\gamma_1+\gamma_c)][(\omega-\omega_2)-i\gamma_2]-\kappa^2}, \tag{A3}$$

with the eigenfrequencies, $\omega_\pm$, given as $\omega_\pm = (1/2)i[-i(\omega_1+\omega_2)+(\gamma_1+\gamma_c+\gamma_2)] \pm (1/2)$

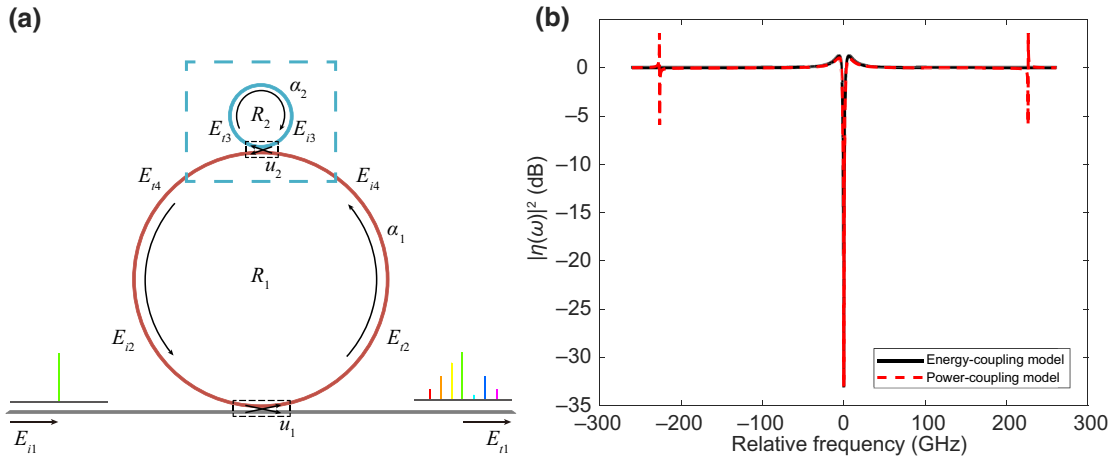

FIG. 6. (a) Power-coupling model. $E_{mn}(m = i, t; n = 1, 2, 3, 4)$ denote the light fields before and after the two couplers between the bus waveguide, main cavity, and auxiliary cavity. (b) $|\eta(\omega)|^2$ calculated by the power-coupling model (red dashed line) and the energy-coupling model (black line). Parameters used in the power-coupling model are $\alpha_1 = 2.4 \times 10^{-3}$, $\alpha_2 = 1.5 \times 10^{-2}$, $u_1 = \sqrt{3.75 \times 10^{-4}}$, $u_2 = 0.021$, $R_1 = 100$ μm, and $R_2 = 3.03$ μm. Parameters used in the energy-coupling model are $\gamma_1 \approx 271.65$ MHz, $\gamma_c \approx 42.45$ MHz, $\gamma_2 \approx 56$ GHz, and $\kappa = 27.3$ GHz.

$\sqrt{4\kappa^2 - [-i(\omega_1 - \omega_2) + (\gamma_1 + \gamma_c - \gamma_2)]^2}$, $\eta(\omega)$ can be simplified as

$$\eta(\omega) = 1 + \frac{\kappa^2}{(\omega - \omega_+)(\omega - \omega_-)}, \tag{A4}$$

in the regime of $\gamma_c \leq \gamma_1$ and $\gamma_1 \ll \gamma_2$, considering the alignment cases, i.e., $\omega_1 = \omega_2$, $\omega_\pm = \omega_1 - i(\gamma_2/2) \pm (1/2)\sqrt{4\kappa^2 - \gamma_2^2}$.

In the power-coupling model [31], the intensity enhancement in the main cavity is

$$\left|\frac{E_{i2}}{E_{i1}}\right|^2 = \left|\frac{iu_1 b_1 \tau_{\mathrm{st}(\omega)} e^{i\phi_1(\omega)}}{1 - r_1 b_1 \tau_{\mathrm{st}(\omega)} e^{i\phi_1(\omega)}}\right|^2, \tag{A5}$$

with the lumped filter term

$$\tau_{\mathrm{st}}(\omega) = \frac{E_{t4}}{E_{i4}} = \frac{r_2 - b_2 e^{i\phi_2(\omega)}}{1 - b_2 r_2 e^{i\phi_2(\omega)}}, \tag{A6}$$

where $b_1 = \exp(-\alpha_1/2)$ and $b_2 = \exp(-\alpha_2/2)$ are the round-trip field-transmission coefficients of the main ring and the auxiliary ring, respectively. r_1 and r_2 are the field-transmission coefficients of the coupling regime, which can be related to u_1 and u_2 by $u_i^2 + r_i^2 = 1$, $i = 1$ or 2, in the lossless coupling approximation. $\phi_i(\omega) = n(\omega_i/c)2\pi R_i$ $(i = 1, 2)$ is the round-trip phase accumulation, where n is the effective mode refractive index and R_i is the radius of the cavity i. As shown in Figs. 2(c)–2(e), Eq. (A2) divided by the round-trip time of the main cavity (i.e., $|a_1/a_0|^2/t_1$) agrees well with Eq. (A5) (i.e., $|E_{i2}/E_{i1}|^2$) due to the difference between the units of a_0 and a_1. The relationships between the parameters of the two models are listed in Table I. As described in the main text, $\tau_{\mathrm{st}}(\omega)$ is the transmission function of the subsystem composed of the auxiliary resonator and part of the main resonator, as shown by the blue dashed box in Fig. 6(a). The intensity enhancement of a single cavity is $|E'_{i2}/E_{i1}|^2 = |iu_1 b_1 e^{i\phi_1(\omega)}/1 - r_1 b_1 e^{i\phi_1(\omega)}|^2$. E'_{i2} denotes the intracavity light field in the single-cavity case. By comparing the intensity enhancement of a single cavity and Eq. (A6), it is easy to see that $\tau_{\mathrm{st}}(\omega)$ is equivalent to a lumped filter inserted into the main cavity. Therefore, $\eta(\omega)$ derived from the TMM can be written as

$$\eta(\omega) = \frac{E_{i2}}{E'_{i2}} = \left[\frac{1 - b_1 r_1 e^{i\phi_1}}{1 - b_1 r_1 \tau_{\mathrm{st}}(\omega) e^{i\phi_1}} \tau_{\mathrm{st}}(\omega)\right]^2. \tag{A7}$$

Figure 6(b) shows the consistency of two models, i.e., Eqs. (A7) and (2) in the main text [or Eq. (A4)]. A perfect match is observed around the target resonance, i.e., relative frequency equals zero when two cavities are aligned. The relative frequency is defined as relative frequency $\omega - \omega_1$. Discrepancies at neighboring resonances are due to the fact that the energy-coupling model is only valid in the vicinity of the target resonance [22].

APPENDIX B: VERIFICATION OF THE GLLE MODEL

The GLLE [12] is used to simulate the generation of DKSs in both normal and anomalous GVD regimes in the main text:

$$t_1 \frac{\partial E}{\partial t} = \left[-\frac{\alpha_1 + u_1^2}{2} - i\delta - iL_1 \sum_{l \geq 2} \frac{\beta_l}{l!}\left(i\frac{\partial}{\partial \tau}\right)^l + i\Gamma L_1 |E|^2\right] E + u_1 E_{\mathrm{in}} + h(\tau) * E, \tag{B1}$$

where E and E_{in} are the envelopes of the intracavity fields of the main cavity and input pump field; δ is the pump phase detuning of the main cavity; β_l and Γ are the dispersion and nonlinear parameters, respectively, and only the second-order dispersion β_2 is considered; $h(\tau)$ is the inverse Fourier transform of the filter function $\tau_{\mathrm{st}}(\omega)$.

To verify the GLLE model, we compare the results from Eq. (B1) with the full-map coupled nonlinear Schrödinger

TABLE I. Relationships between the parameters of the power-coupling model and the energy-coupling model.

Power-coupling model		Energy-coupling model		Conversion or relationship
Field-coupling coefficient between waveguide and main ring	u_1	Coupling-induced energy decay rate	γ_c	$\gamma_c = \frac{u_1^2}{2t_1}$
Field-coupling coefficient between two rings	u_2	Energy-coupling rate	κ	$u_2 = \kappa\sqrt{t_1 t_2}$
Field-transmission coefficient of coupling region	r_i	–	–	$u_i^2 + r_i^2 = 1$
Round-trip field-transmission coefficient	b_i	Intrinsic energy decay rate of cavity i	γ_i	$b_i = e^{-\gamma_i t_i}$
Intrinsic loss per round trip	α_i			$\alpha_i = 2\gamma_i t_i$

equations [40]:

$$\frac{\partial A_1}{\partial z} = \left[-\alpha_{i1}^s - i\delta_1^s - \Delta k'^s \frac{\partial}{\partial \tau} - i\frac{k_1''^s}{2}\frac{\partial^2}{\partial \tau^2} + i\Gamma_1^s |A_1|^2\right] A_1 + \sum_{n=-\infty}^{+\infty} \delta(z - nL)[iu_1 A_{\text{in}} - (1 - r_1)A_1] + \sum_{n=-\infty}^{+\infty} \delta\left(z - nL - \frac{L}{2}\right)[iu_2 A_2 - (1 - r_2)A_1], \tag{B2a}$$

$$\frac{\partial A_2}{\partial z} = \left[-\alpha_{i2} - i\delta_2 - i\frac{k''_2}{2}\frac{\partial^2}{\partial \tau^2} + i\Gamma_2 |A_2|^2\right] A_2 + \sum_{n=-\infty}^{+\infty} \delta\left(z - nL - \frac{L}{2}\right)[iu_2 A_1 - (1 - r_2)A_2], \tag{B2b}$$

where A_{in}, A_1, and A_2 are the complex field amplitudes of the pump, the main cavity, and the auxiliary cavity, respectively; z is the propagation distance in the cavities. Subscripts 1 and 2 represent the main cavity and the auxiliary cavity, respectively, and superscript "s" represents the correspondingly scaled parameters between the main and auxiliary cavity. $\alpha_{i1}^s = (\alpha_1/2L_1)(L_1/L_2)$ and $\alpha_{i2} = \alpha_2/2L_2$ are the intrinsic amplitude losses per unit length; $\delta_1^s = (m_1 2\pi - k_1^s L_2)/L_2$ and $\delta_2 = (m_2 2\pi - k_2 L_2)/L_2$ are the phase detuning per unit length; $m_{1,2}$ are the mode numbers of the cavity modes that are pumped; $k_{1,2}$ are the wave vectors with $k_1^s = k_1(L_1/L_2)$; $k'_{1,2} = dk_{1,2}/d\omega|_{\omega=\omega_p}$ are the reciprocals of the group velocities at the pump angular frequency (ω_p) and $\Delta k'^s = k'_1(L_1/L_2) - k'_2$ is the group-velocity mismatch; $k_1''^s = \beta_2(L_1/L_2)$ and $k''_2 = \beta_2$ are the group-velocity dispersions; $\Gamma_1^s = \Gamma(L_1/L_2)$ and $\Gamma_2 = \Gamma$ are nonlinear parameters; $\delta(\cdot)$ is the Dirac function; $L = L_2$. The linear performance of this full-map model can be compared with the TMM by setting the nonlinear parameter to zero. The transmission spectrum and intensity enhancements in the main cavity derived by the full-map model agree well with that of the TMM, as shown in Fig. 7.

Figures 8(a)–8(f) show the results obtained from Eqs. (B2) and (B1) under different L_1/L_2. The single-soliton state obtained by the two models agrees well in all cases. The periodic depletion features on the comb spectra are simply due to the fact that L_1 divided by L_2 is an integer.

Figure 9 illustrates the power distributions in the auxiliary cavity, including the temporal waveforms [Figs. 9(a) and 9(d)], spectra [Figs. 9(b) and 9(e)], and the normalized power traces as a function of the scanning time [Figs. 9(c) and 9(f)], in cases of the anomalous and normal GVD regimes. This reveals that the power distribution in the auxiliary ring (blue lines) is much less than that in the main ring (red lines), and no soliton exists in the auxiliary cavity. Unlike the coupled photonic dimer with an identical radius [34], in this study, the radiation decay of the auxiliary cavity is much larger than the main cavity. So the intensity is smaller, and the nonlinearity is weaker in the auxiliary cavity.

APPENDIX C: TUNABLE OPTICAL FREQUENCY COMBS WITH DISPERSION-SUPPRESSED MODE DEPLETION

Figure 10 shows the Kerr optical frequency combs generated with tunable mode depletion. Figures 10(a)–10(c) show that the situations when the dispersion-suppressed

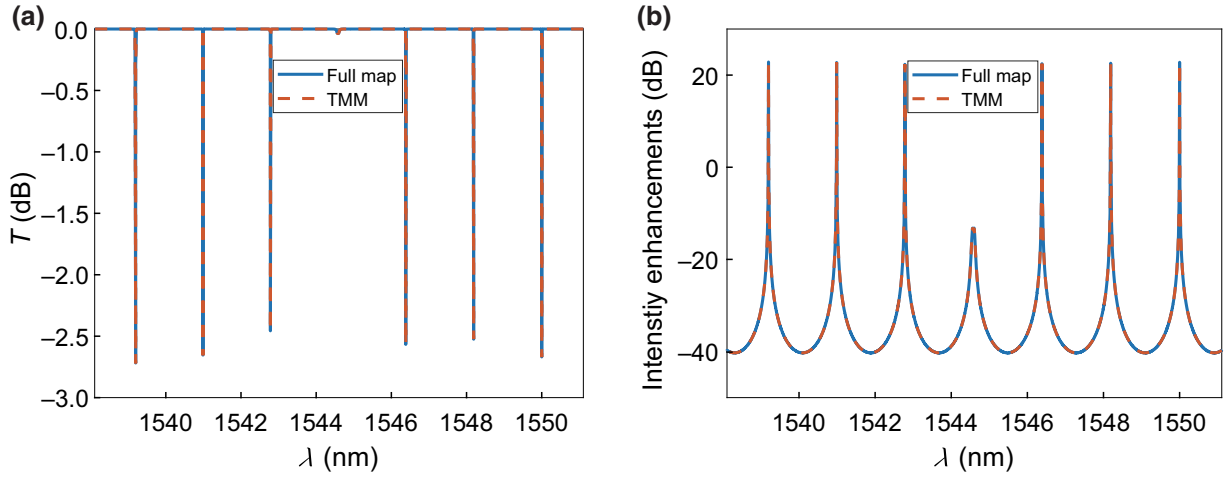

FIG. 7. Consistency of full map and TMM. (a) Transmission spectrum of the coupled microring resonators. Blue line is the result of the full-map model, and red dashed line is calculated by the TMM. (b) Intensity enhancements of the main cavity of the coupled microring resonators. Blue line and red dashed line are calculated by the full-map model and TMM, respectively. Parameters of the structure are the same as those in Fig. 4.

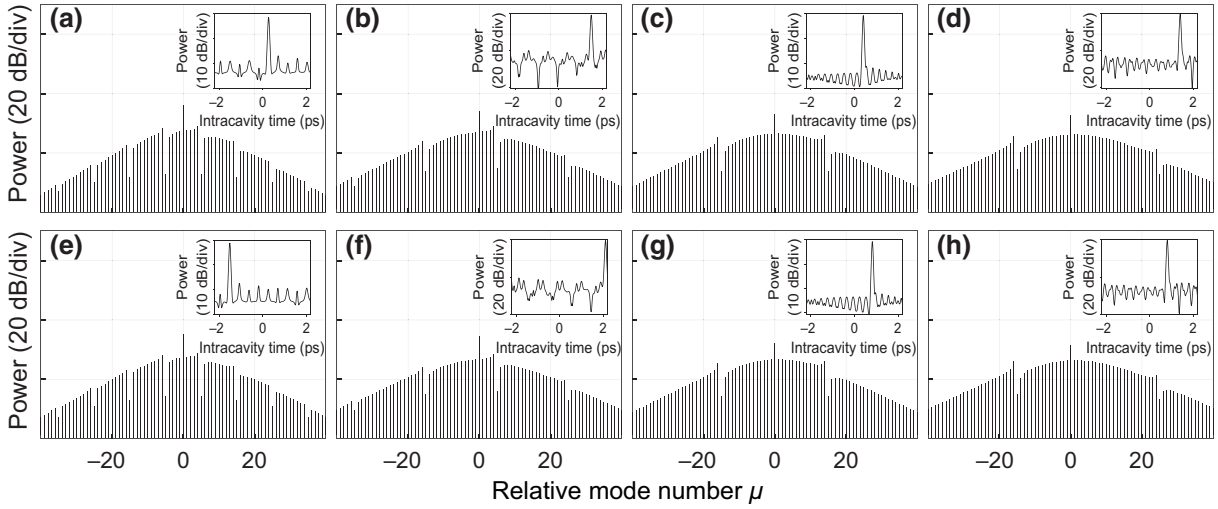

FIG. 8. Optical spectra as well as the temporal waveform of the single-soliton state using full map (a)–(d) or GLLE (e)–(h) model. $L_1/L_2 = 10,\ 20,\ 30,$ and 40 are used in (a),(e); (b),(f); (c),(g); and (d),(h), respectively. Parameters used for both models are the same: $t_1 = 4.4$ ps, $L_1 = 628\ \mu$m, $\alpha_1 = 2.4 \times 10^{-3}$, $\alpha_2 = 5 \times 10^{-2}$, $u_1 = \sqrt{3.75 \times 10^{-4}}$, $u_2 = 0.049$, $\beta_2 = -81$ ps^2/km, $\Gamma = 1$(W m)$^{-1}$, and $|E_{\text{in}}|^2 = 0.42$ W. δ scans linearly starting from -0.0041 at a sweep rate of 7.55×10^{-7} per round trip.

mode depletion brought by $\tau_{\text{st}}(\omega)$ are tuned to the third, fourth, and fifth modes compared to the pump mode, respectively. For the main microresonator, which is operated in the anomalous GVD regime, as shown in Figs. 10(a)-i2–10(c)-i2, it is evident that relative modes $\mu = 3$, 4, and 5 suffer from significant depletion due to the dispersion-suppressed mode-depletion effect. Meanwhile, the intracavity solitons in Figs. 10(a)-i1–10(c)-i1 also generate an oscillating tail with periodicity in accordance with the relative mode index [41]. For the main microresonator in the normal GVD regime, the generated frequency combs are shown in Figs. 10(a)-ii2–10(c)-ii2, with comb spacing equal to 3, 4, and 5 times the FSR of the main cavity, respectively. In the

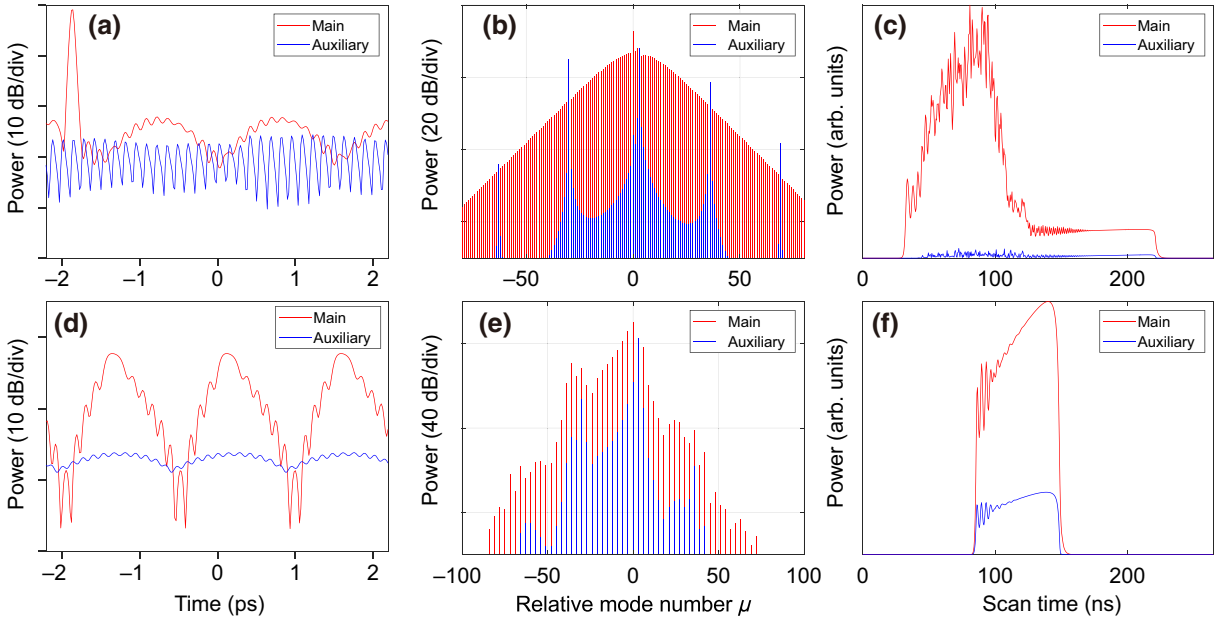

FIG. 9. Comparison of the power distribution in the main ring and auxiliary ring; in the case of the resonant mode, $\mu = 3$ of the main ring is aligned with the auxiliary ring, under the conditions of (a)–(c) the anomalous dispersion regime and (d)–(f) the normal dispersion regime; (a),(d); (b),(e); and (c),(f) show the temporal waveform, optical spectra, and the normalized power trace when scanning the laser to introduce solitons in both the main (red) and auxiliary (blue) cavities, respectively. Parameters used in (a)–(c),(b)–(d) are identical to those of Figs. 4 and 5, respectively.

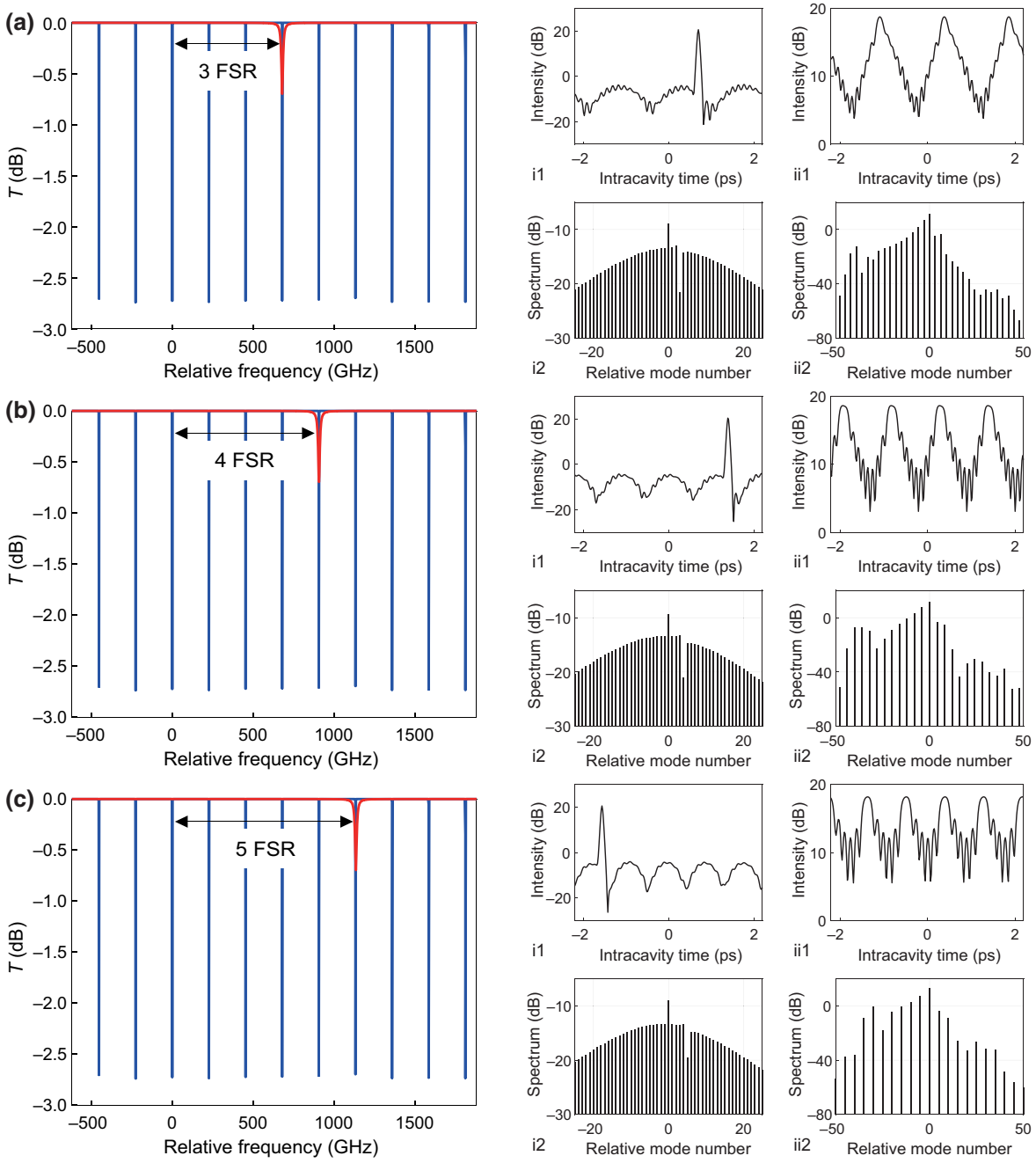

FIG. 10. Tunability of optical frequency comb. (a)–(c) Depleted mode is tuned to the third, fourth, and fifth mode corresponding to the pump mode, respectively. Blue line is the transmission spectrum of the single main cavity without the coupled auxiliary cavity, and the red line is $|\tau_{st}(\omega)|^2$. (a)–(c)i1 and (a)–(c)i2 are the simulated temporal soliton and the corresponding spectrum in anomalous dispersion. (a)–(c)ii1 and (a)–(c)ii2 are the simulated temporal waveform and the corresponding spectrum in normal dispersion. Parameters used are the same as Fig. 4 in anomalous dispersion and Fig. 5 in normal dispersion.

meantime, the corresponding temporal waveforms are shown in Figs. 10(a)-ii1–10(c)-ii1, respectively, with three, four, and five dark pulses generated within one round-trip time. In brief, the mode that gets depleted can be tuned so that the frequency combs generated in the anomalous or normal dispersion regions can be tuned by adjusting the depleted mode.

APPENDIX D: GENERATION OF OCTAVE-SPANNING FREQUENCY COMBS

Optical solitons can emit Cherenkov radiation in the presence of higher-order dispersion. This process allows a substantial increase in the spectral bandwidth of pulsed laser sources and even the generation of octave-spanning

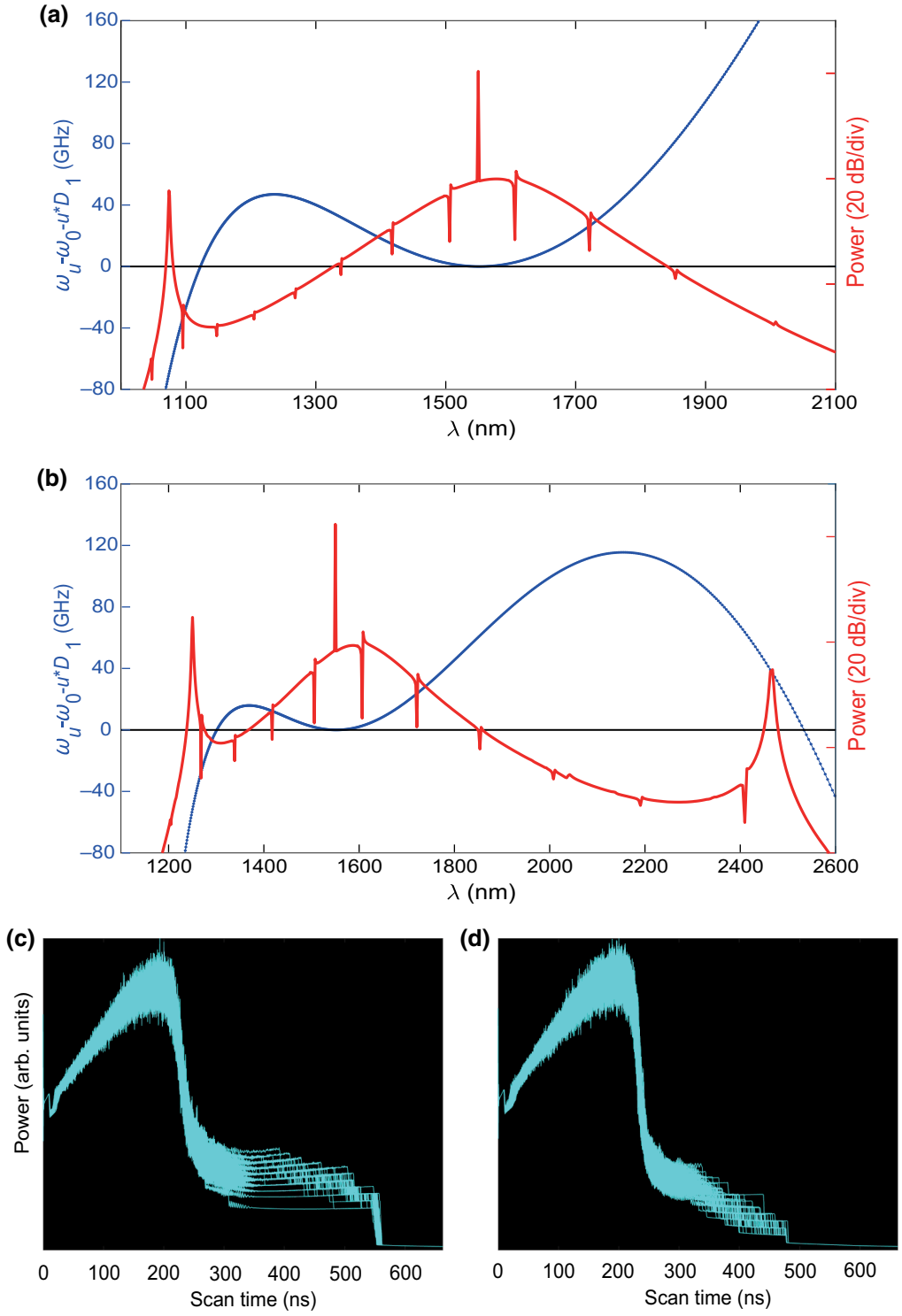

FIG. 11. Spectra of optical frequency comb of single soliton (solid red line) and local dispersion (blue dotted line) in the main cavity considering dispersion up to the third- (a) and fourth- (b) order dispersions. Left axis corresponds to local dispersion (blue dotted line), and the right axis corresponds to the power of the spectra (solid red line). (c),(d) 100 overlaid normalized power traces obtained without and with single-mode depletion considering the third-order dispersion. Simulation parameters are $t_{R_1} = 4.4$ ps, $L_1 = 628$ μm, $\alpha_1 = 9 \times 10^{-3}$, $\alpha_2 = 2 \times 10^{-2}$, $u_1 = \sqrt{9 \times 10^{-3}}$, $u_2 = 0.042$, $\beta_2 = -20$ ps^2/km, $\beta_3 = -0.129$ ps^3/km, $\beta_4 = 2.18 \times 10^{-3}$ ps^4/km, $\Gamma = 1(\mathrm{W\ m})^{-1}$, and $|E_{\mathrm{in}}|^2 = 1.11$ W. δ scans linearly starting from -0.0045 at the sweep rate of 9×10^{-7} per round-trip. The circumference ratio of the main cavity and the auxiliary cavity is 55.

frequency combs [42]. Regarding the discussion in the main text, only the second-order dispersion is considered. In this appendix, the impact of higher-order dispersion is considered, including third or even fourth order, which shows the potential of our scheme in the generation of broadband frequency combs or octave-spanning frequency combs. Figure 11 illustrates the envelope of optical frequency combs (solid red line) with mode depletion, and local dispersion of the main cavity when the third-order dispersion [Fig. 11(a)] and even the fourth-order dispersion [Fig. 11(b)] are taken into account. Figures 11(c) and 11(d) show 100 overlaid normalized power traces obtained in the case of a single main cavity and our *PT*-symmetry structure, respectively, with the same pump scanning rate. Third-order dispersion is considered in this case. It is clear that the probability of single-soliton generation in the situation of the octave-spanning frequency-comb generation can be boosted, with the existence period of the single-soliton step being significantly extended.

APPENDIX E: GREATLY IMPROVED SINGLE-SOLITON GENERATION

The impact of the pump detuning rate, the loss of the auxiliary cavity, coupling, and misalignment between two cavities on the probability of single-soliton formation is given in Fig. 12. Figures 12(a) and 12(b) show diagrams of the probability of single-soliton generation without and with single-mode depletion as a function of pump detuning and unidirectional pump scanning rate, respectively. It can be seen that, without dispersion-suppressed mode depletion, the single-soliton-generation probability does not have a significant improvement, no matter what the scanning rate is. However, single-soliton formation is significantly facilitated at a wide range of pump scanning rates with the help of mode depletion. Figures 12(c)–12(e) show the impact of single-soliton-generation probability as a function of the auxiliary cavity loss, α_2; coupling coefficient, u_2 (between two cavities); and detuning (or misalignment) between the two cavities. It can be seen

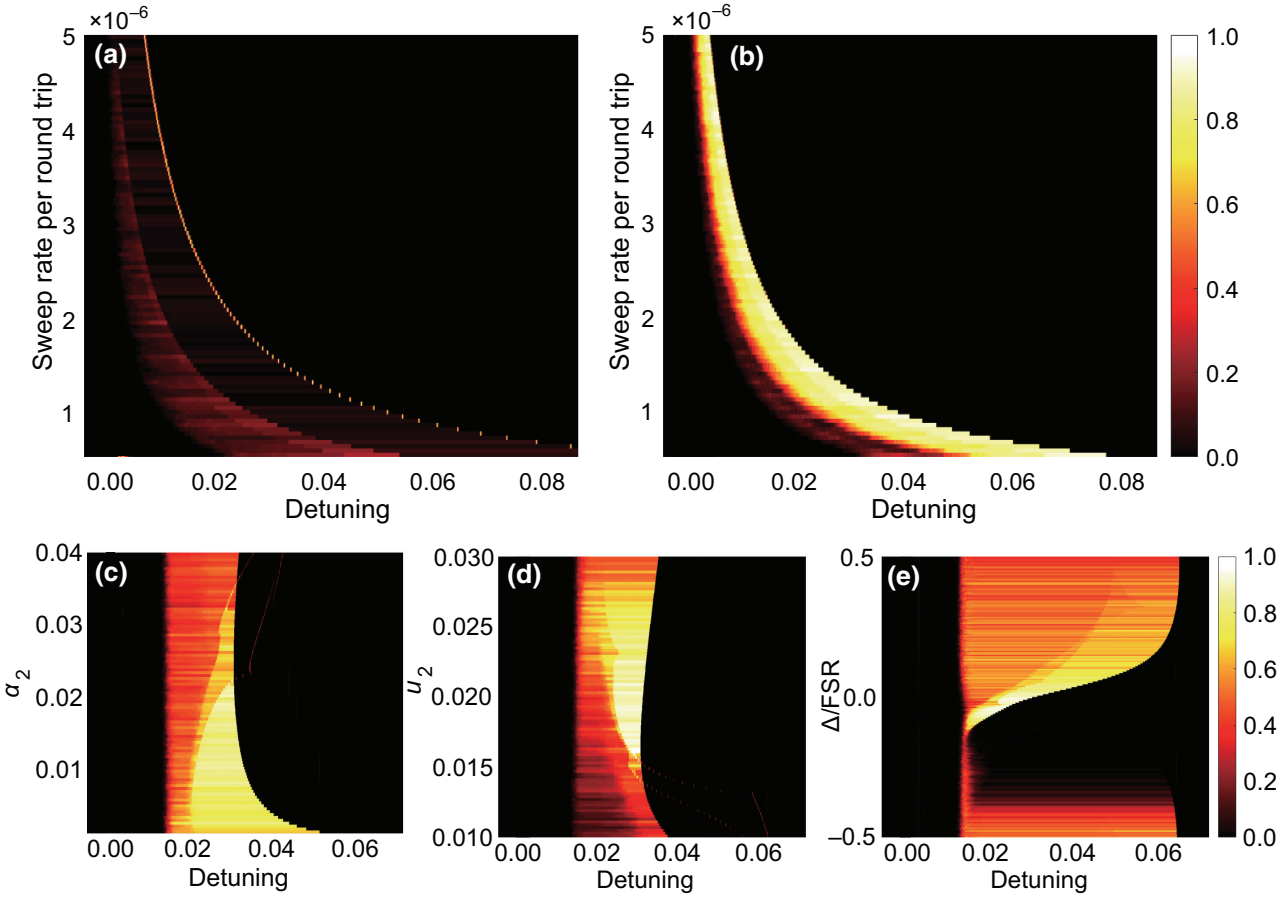

FIG. 12. Probability of single-soliton formation without (a) and with (b)–(e) dispersion-suppressed mode depletion as a function of (a),(b) unidirectional pump scanning rate; (c) loss of auxiliary cavity α_2; (d) coupling coefficient u_2; and (e) detuning between two cavities, i.e., $\Delta = \omega_2 - \omega_1$, in the anomalous GVD regime. Parameters used are the same as those in Fig. 4 except $|E_{\rm in}|^2 = 0.32$ W.

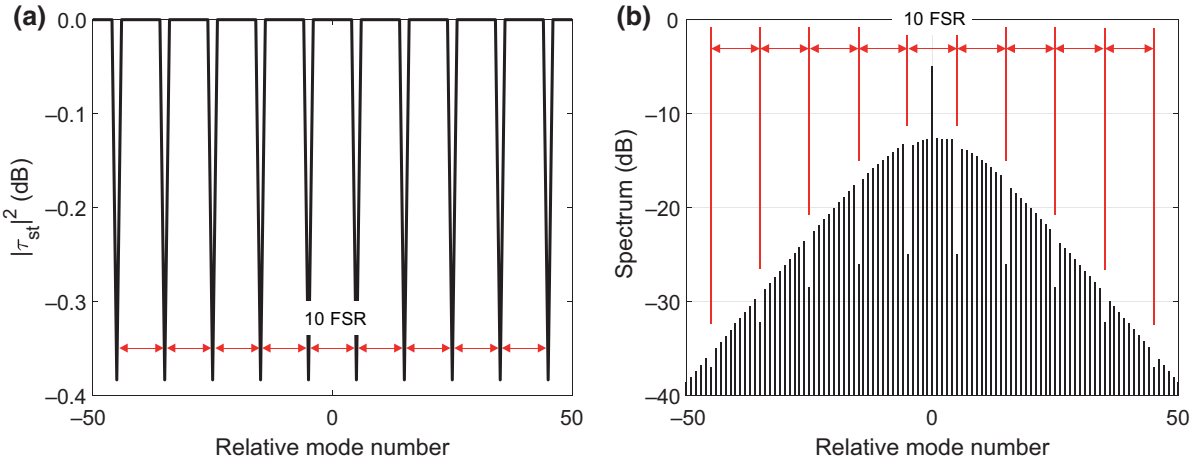

FIG. 13. Impact of the periodicity of $\tau_{st}(\omega)$. (a) $|\tau_{st}(\omega)|^2$ with a period of 10 FSR (main cavity). (b) Simulated spectrum with $\tau_{st}(\omega)$ shown in (a). Parameters used are the same as those in Fig. 4 except L_1/L_2 is 10.

that single-soliton generation with high probability shows great robustness against various parameters. In particular, improvement of soliton generation occurs even with a large misalignment between the two cavities, indicating the role of dispersion-induced single-soliton generation in the misaligned case [33].

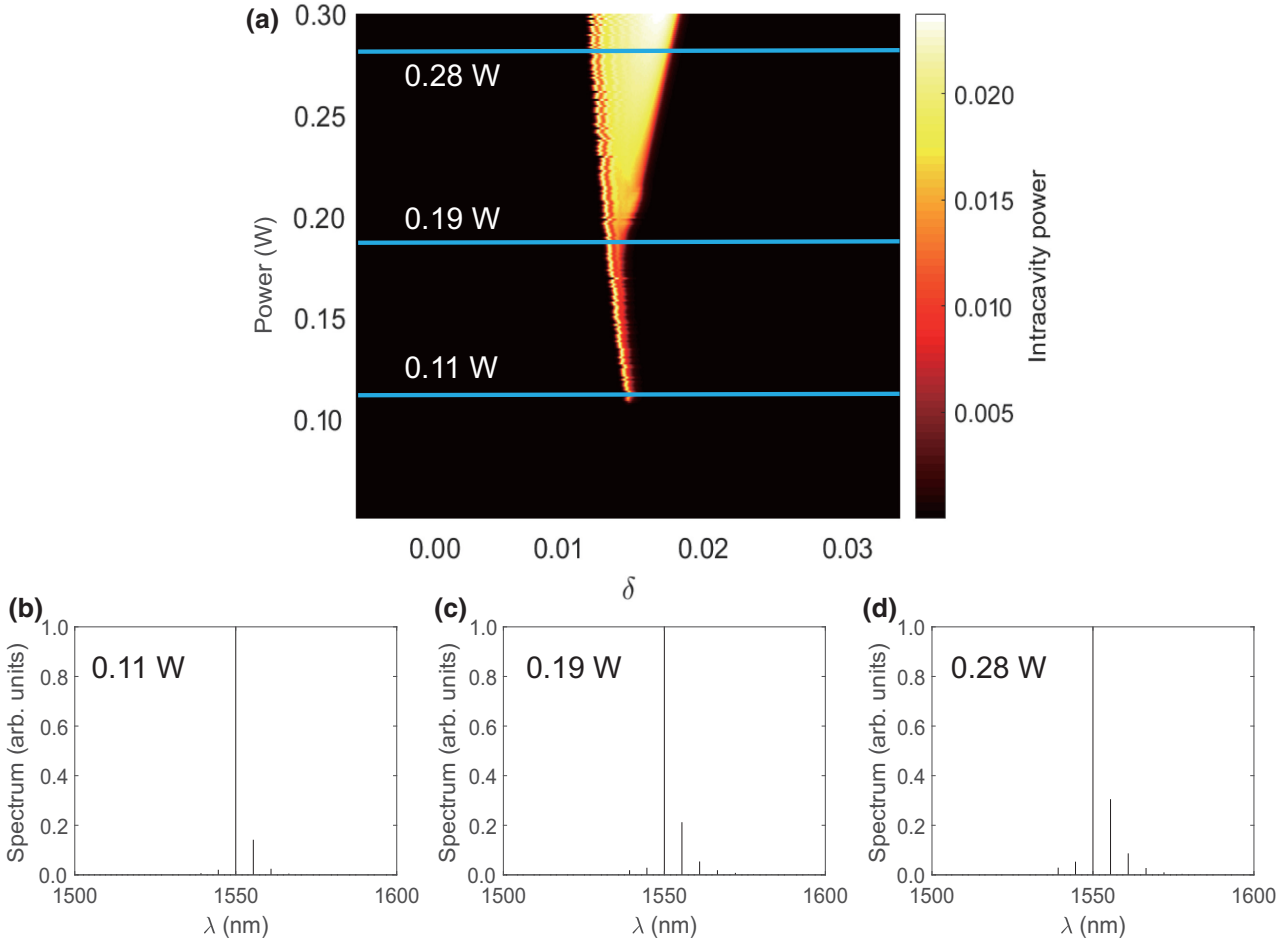

FIG. 14. Analysis of the threshold of MI induced by dispersion-suppressed mode depletion in normal GVD microresonators. (a) Intracavity power (all comb lines except the pump line are considered) as a function of the pump power and pump detuning under the parameters of Fig. 5. (b)–(d) Intracavity spectra with input pump power at 0.11, 0.19, and 0.28 W, respectively.

APPENDIX F: THE IMPACT OF THE PERIODICITY OF $\tau_{st}(\omega)$

When the radius of the auxiliary cavity is approximately infinite, it can be regarded as an absolute single-mode depletion. However, in the actual situation, single-mode depletion is valid over a specific bandwidth due to the physical limitations in decreasing the radius of the auxiliary cavity. Therefore, $\tau_{st}(\omega)$ related to the auxiliary cavity is periodic. Figure 13(a) shows $\tau_{st}(\omega)$ with a period of 10 FSR (FSR in the main cavity). As a result, the dispersion-suppressed mode depletion occurs every ten modes of the main resonances.

APPENDIX G: THRESHOLD ANALYSIS OF THE MODULATION INSTABILITY IN THE NORMAL GVD REGIME

The intracavity power (all comb lines except the pump line are considered) as a function of the pump power and pump detuning under the parameters of Fig. 5 is given in Fig. 14(a). The intracavity spectra with pump powers of 0.11, 0.19, and 0.28 W are given in Figs. 14(b)–14(d), respectively. It can be seen that the input pump threshold is about 0.11 W to generate the MI state.

APPENDIX H: LOCAL DISPERSION OF THE SITUATION DISCUSSED IN Fig. 5

The local dispersion is defined as $D_{int}(\mu) = \omega_\mu - \omega_0 - D_1\mu$, where D_1 and μ correspond to the FSR of the main cavity and the relative mode index of the main cavity with respect to ω_0, respectively [36]. ω_0 is the central pump frequency with $\mu = 0$, and ω_μ represents the frequency over the relative mode index, μ, of the main cavity. Figure 15 shows the local dispersion of the situation discussed in Fig. 5. It is evident that all modes remain in the normal GVD regime. In this case, the MI state cannot be introduced, resulting in the absence of the sideband shown in Fig. 5(b).

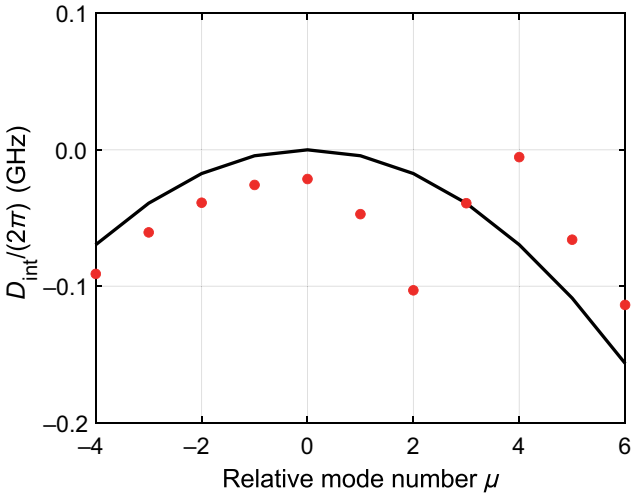

FIG. 15. Local dispersion of the situation discussed in Fig. 5.

[1] P. Marin-Palomo, J. Kemal, M. Karpov, A. Kordts, J. Pfeifle, M. H. P. Pfeiffer, P. Trocha, S. Wolf, V. Brasch, M. H. Anderson, *et al.*, Microresonator-based solitons for massively parallel coherent optical communications, Nature **546**, 274 (2017).

[2] J. S. Levy, A. Gondarenko, M. Foster, Amy C. Turner-Foster, Alexander L. Gaeta, and M. Lipson, CMOS-compatible multiple-wavelength oscillator for on-chip optical interconnects, Nat. Photonics **4**, 37 (2010).

[3] Z. Ye, P. Zhao, K. Twayana, M. Karlsson, V. Torres-company, and P. A. Andrekson, Overcoming the quantum limit of optical amplification in monolithic waveguides, Sci. Adv. **7**, 38 (2021).

[4] M. Pu, H. Hu, L. Ottaviano, E. Semenova, D. Vukovic, L. K. Oxenløwe, and K. Yvind, Ultra-efficient and broadband nonlinear AlGaAs-on-insulator chip for low-power optical signal processing, Laser Photonics Rev. **12**, 1800111 (2018).

[5] E. Obrzud, M. Rainer, A. Harutyunyan, M. H. Anderson, J. Liu, M. Geiselmann, B. Chazelas, S. Kundermann, S. Lecomte, M. Cecconi, *et al.*, A microphotonic astrocomb, Nat. Photonics **13**, 31 (2019).

[6] J. Liu, E. Lucas, A. S. Raja, J. He, J. Riemensberger, R. N. Wang, M. Karpov, H. Guo, R. Bouchand, and T. J. Kippenberg, Photonic microwave generation in the X- and K-band using integrated soliton microcombs, Nat. Photonics **14**, 486 (2020).

[7] M. Kues, C. Reimer, P. Roztocki, L. R. Cortés, S. Sciara, B. Wetzel, Y. Zhang, A. Cino, S. T. Chu, B. E. Little, *et al.*, On-chip generation of high-dimensional entangled quantum states and their coherent control, Nature **546**, 622 (2017).

[8] M. E. Marhic, *Fiber Optical Parametric Amplifiers, Oscillators and Related Devices* (Cambridge University Press, New York, 2007).

[9] S. Kim, K. Han, C. Wang, J. A. Jaramillo-Villegas, X. Xue, C. Bao, Y. Xuan, D. E. Leaird, A. M. Weiner, and M. Qi, Dispersion engineering and frequency comb generation in thin silicon nitride concentric microresonators, Nat. Commun. **8**, 372 (2017).

[10] R. El-Ganainy, J. I. Dadap, and R. M. Osgood, Optical parametric amplification via non-Hermitian phase matching, Opt. Lett. **40**, 5086 (2015).

[11] T. Tanemura, Y. Ozeki, and K. Kikuchi, Modulational Instability and Parametric Amplification Induced by Loss Dispersion in Optical Fibers, Phys. Rev. Lett. **93**, 163902 (2004).

[12] A. M. Perego, S. K. Turitsyn, and K. Staliunas, Gain through losses in nonlinear optics, Light Sci. Appl. **7**, 1 (2018).

[13] X. Guo, C. Zou, L. Jiang, and H. X. Tang, All-Optical Control of Linear and Nonlinear Energy Transfer via the Zeno Effect, Phys. Rev. Lett. **120**, 203902 (2018).

[14] Y. H. Wen, O. Kuzucu, M. Fridman, A. L. Gaeta, L. Luo, and M. Lipson, All-Optical Control of an Individual

Resonance in a Silicon Microresonator, Phys. Rev. Lett. **108**, 223907 (2012).
[15] Y. H. Wen, O. Kuzucu, T. Hou, M. Lipson, and A. L. Gaeta, All-optical switching of a single resonance in silicon ring resonators, Opt. Lett. **36**, 1413 (2011).
[16] T. Tanemura, Y. Takushima, and K. Kikuchi, Narrowband optical filter, with a variable transmission spectrum, using stimulated Brillouin scattering in optical fiber, Opt. Lett. **27**, 1552 (2002).
[17] F. Bessin, A. M. Perego, K. Staliunas, S. K. Turitsyn, A. Kudlinski, M. Conforti, and A. Mussot, Gain-through-filtering enables tuneable frequency comb generation in passive optical resonators, Nat. Commun. **10**, 4489 (2019).
[18] X. Xue, Y. Xuan, P. Wang, Y. Liu, D. E. Leaird, M. Qi, and A. M. Weiner, Normal-dispersion microcombs enabled by controllable mode interactions, Laser Photonics Rev. **9**, L23 (2015).
[19] S. A. Miller, Y. Okawachi, S. Ramelow, K. Luke, A. Dutt, A. Farsi, A. L. Gaeta, and M. Lipson, Tunable frequency combs based on dual microring resonators, Opt. Express **23**, 21527 (2015).
[20] M. Soltani, A. Matsko, and L. Maleki, Enabling arbitrary wavelength frequency combs on chip, Laser Photonics Rev. **10**, 158 (2016).
[21] H. Hodaei, M.-A. Miri, M. Heinrich, D. N. Christodoulides, and M. Khajavikhan, Parity-time–symmetric microring lasers, Science **346**, 975 (2014).
[22] B. Peng, Ş. K. Özdemir, F. Lei, F. Monifi, M. Gianfreda, G. L. Long, S. Fan, F. Nori, C. M. Bender, and L. Yang, Parity–time-symmetric whispering-gallery microcavities, Nat. Phys. **10**, 394 (2014).
[23] B. Peng, Ş. K. Özdemir, S. Rotter, H. Yilmaz, M. Liertzer, F. Monifi, C. M. Bender, F. Nori, and L. Yang, Loss-induced suppression and revival of lasing, Science **342**, 328 (2014).
[24] A. A. Mailybaev, J. Böhm, J. Böhm, U. Kuhl, A. Girschik, F. Libisch, T. J. Milburn, P. Rabl, N. Moiseyev, and S. Rotter, Dynamically encircling an exceptional point for asymmetric mode switching, Nature **537**, 76 (2016).
[25] H. Xu, D. Mason, L. Jiang, and J. G. E. Harris, Topological energy transfer in an optomechanical system with exceptional points, Nature **537**, 80 (2016).
[26] H. Hodaei, A. U. Hassan, S. Wittek, H. Garcia-Garcia, R. El-Ganainy, D. N. Christodoulides, and M. Khajavikhan, Enhanced sensitivity at higher-order exceptional points, Nature **548**, 187 (2017).
[27] Y. H. Lai, Y. K. Lu, M. G. Suh, Z. Yuan, and K. Vahala, Observation of the exceptional-point-enhanced Sagnac effect, Nature **576**, 65 (2019).
[28] M. P. Hokmabadi, A. Schumer, D. N. Christodoulides, and M. Khajavikhan, Non-Hermitian ring laser gyroscopes with enhanced Sagnac sensitivity, Nature **576**, 70 (2019).
[29] C. Milián, Y. V. Kartashov, D. V. Skryabin, and L. Torner, Cavity solitons in a microring dimer with gain and loss, Opt. Lett. **43**, 979 (2018).
[30] K. Komagata, A. Tikan, A. Tusnin, J. Riemensberger, M. Churaev, H. Guo, and T. J. Kippenberg, Dissipative Kerr solitons in a photonic dimer on both sides of exceptional point, Commun. Phys. **4**, 159 (2021).
[31] V. Van, in *Optical Microring Resonators: Theory, Techniques, and Applications*, 1st ed. (CRC Press, Boca Raton, 2016).
[32] T. J. Kippenberg, A. L. Gaeta, M. Lipson, and M. L. Gorodetsky, Dissipative Kerr solitons in optical microresonators, Science **361**, enna8083 (2018).
[33] C. Bao, Y. Xuan, D. E. Leaird, S. Wabnitz, M. Qi, and A. M. Weiner, Spatial mode-interaction induced single soliton generation in microresonators, Optica **4**, 1011 (2017).
[34] A. Tikan, J. Riemensberger, K. Komagata, S. Hönl, M. Churaev, C. Skehan, H. Guo, R. N. Wang, J. Liu, P. Seidler, and T. J. Kippenberg, Emergent nonlinear phenomena in a driven dissipative photonic dimer, Nat. Phys. **17**, 604 (2021).
[35] H. Guo, M. Karpov, E. Lucas, A. Kordts, M. H. P. Pfeiffer, V. Brasch, G. Lihachev, V. E. Lobanov, M. L. Gorodetsky, and T. J. Kippenberg, Universal dynamics and deterministic switching of dissipative Kerr solitons in optical microresonators, Nat. Phys. **13**, 94 (2017).
[36] T. Herr, V. Brasch, J. D. Jost, I. Mirgorodskiy, G. Lihachev, M. L. Gorodetsky, and T. J. Kippenberg, Mode Spectrum and Temporal Soliton Formation in Optical Microresonators, Phys. Rev. Lett. **113**, 123901 (2014).
[37] X. Xue, Y. Xuan, Y. Liu, P. Wang, S. Chen, J. Wang, D. E. Leaird, M. Qi, and A. M. Weiner, Mode-locked dark pulse Kerr combs in normal-dispersion microresonators, Nat. Photonics **9**, 594 (2015).
[38] Y. Liu, Y. Xuan, X. Xue, P. Wang, S. Chen, A. J. Metcalf, J. Wang, D. E. Leaird, M. Qi, and A. M. Weiner, Investigation of mode coupling in normal-dispersion silicon nitride microresonators for Kerr frequency comb generation, Optica **1**, 137 (2014).
[39] H. Hu, L. Zhang, C. Zhang, Y. Chen, J. Xu, and X. Zhang, Lumped dissipation induced quasi-phase matching for broad and flat optical parametric processes, IEEE Photonics J. **11**, 1 (2019).
[40] X. Xue, X. Zheng, and B. Zhou, Super-efficient temporal solitons in mutually coupled optical cavities, Nat. Photonics **13**, 616 (2019).
[41] Y. Wang, F. Leo, J. Fatome, M. Erkintalo, S. G. Murdoch, and S. Coen, Universal mechanism for the binding of temporal cavity solitons, Optica **4**, 855 (2017).
[42] Q. Li, T. C. Briles, D. A. Westly, T. E. Drake, J. R. Stone, B. R. Ilic, S. A. Diddams, S. B. Papp, and K. Srinivasan, Stably accessing octave-spanning microresonator frequency combs in the soliton regime, Optica **4**, 193 (2017).